AN ERTS MULTISPECTRAL SCANNER EXPERIMENT FOR MAPPING IRON COMPOUNDS

Robert K. Vincent

Willow Run Laboratories
The University of Michigan
Ann Arbor, Michigan

1. INTRODUCTION

Last year a thermal infrared ratio imaging technique was developed for mapping gross variations in $\%SiO_2$ content among silicate rock types from airborne thermal infrared scanner data [1, 2, 3]. That technique capitalized on spectral emittance features caused by molecular vibrations of the silicon-oxygen ions in SiO_4 tetrahedra of silicate minerals and rocks. More recently a similar ratio imaging technique has been applied to airborne multispectral scanner data in the visible-reflective infrared wavelength region for mapping variations in iron compounds [4]. That wavelength region contains spectral reflectance features which are caused primarily by electronic transitions in the outer electron shells of ferric and ferrous ions. The purpose of this paper is to describe an experiment designed to produce visible-reflective infrared ratio images from ERTS satellite data. Although no ERTS data have yet been processed in this study, the experimental plan is published here to assist other ERTS investigators, in both geology and other scientific disciplines, who may find this data processing method useful.

2. BACKGROUND

Iron compounds are promising remote sensing targets because they display prominent spectral features in the visible-reflective infrared wavelength region and are geologically significant. For example, iron oxides are weathering products of mafic minerals, by-products of hydrothermal alteration, and residual constituents of lateritic soils. Thus a method for monitoring ferric and/or ferrous oxides should contribute to remote sensing efforts concerned with regional geologic mapping, exploration for new mineral resources, and classification of soils.

The spectral features of iron oxides in the wavelength region below approximately 2.0μm are caused by electronic transitions of the Fe^{+2} ferrous ion (at 1.0μm, 0.55μm, 0.51μm, 0.45μm, and 0.43μm) and the Fe^{+3} ferric ion (at 0.87μm, 0.70μm, and 0.40μm) [5]. These electronic transitions produce spectral reflectance minima, the most prominent of which occur near 1.0μm for ferrous compounds and near 0.87μm and 0.70μm for ferric compounds. The reflectance minima of ferric oxides are preceded on the short wavelength side by a spectral reflectance curve of positive slope.

As mentioned above, a ratio image technique exploiting the spectral features of iron compounds has been applied to aircraft data. The data were collected by the University of Michigan's M-7 multispectral scanner on 30 October 1971 approximately 1 hour after sunrise at an above-ground altitude of approximatley 1 km over Pisgah Crater, California. From the Pisgah

Crater data it was possible to produce analog ratio images by dividing the radiances in two spectral channels of information, and using the resulting ratio as an input signal to an analog computer. Figure 1 shows two single channel images and a ratio image of an area covered by a north-south flight line over Pisgah Crater, which is located in the right-hand portion of each of the three images in this figure. Three eruptive phases (labeled in Fig. 1 as 1, 2 and 3) of basaltic lava which flowed from Pisgah Crater in the late Pleistocene or early Recent epochs appear in the right half of the images. Chemically, the three phases of lava have approximately the same SiO_2 content, but vary in Fe_2O_3 and FeO content. Texturally, the two phases are quite different; phase 2 lava is primarily aa (blocky) and phase 3 is pahoehoe (ropey).

In the ratio image of Figure 1, there are large gray level variations near Pisgah Crater which are not noticeable in the single channel images. Phase 3 lava appears darker than windblown sand (S) in the ratio image, but brighter than phase 2 lava. Phase 2 lava appears much darker (smaller ratio) than the windblown sand, and phase 1 lava appears darker than either of the other two eruptive phases in the ratio image.

Figure 2 shows the mean spectral reflectance curves of several lava (basalt) samples gathered from each of the three eruptive phases. These measurements were made on a Beckman spectrophotometer with an integrating sphere attachment. Though the standard deviations of each mean curve are large, a ratio of average reflectances in the two designated scanner spectral channels indicates that the ratios should be highest (0.743) for the youngest phase 3 lava, intermediate (0.579) for phase 2, and lowest (0.457) for the oldest phase 1. Both observations agree qualitatively with the scanner ratio image of figure 1, i.e., there are ratio image variations within each eruptive phase, but on the average, the relative values in the ratio image decrease from phase 3 to phase 2 to phase 1 lava. This indicates that the ratios measured by channels 5 and 7 of the airborne scanner can be used to monitor spectral variations relating to chemical composition of exposed rock surfaces, in spite of the fact that shadowing, scan-angle effects, and target geometry variations are present across the scene.

Rapid rock analysis has been performed on only two of the above basaltic lava samples. They showed a phase 3 sample to have bulk weight-percent of 2.1% Fe_2O_3 and 8.1% FeO, and a phase 1 sample to have 2.2% Fe_2O_3 and 7.9% FeO. Although this would indicate that higher bulk Fe O content may correspond to a lower aircraft channel 5 to channel 7 ratio, many more chemical analyses would be necessary to verify this relationship.

The ERTS-A multispectral scanner has two channels in the visible-reflective infrared wavelength region which should be capable of duplicating the aircraft scanner results. Table I shows the average reflectances in the four ERTS-A MSS spectral bands for a few minerals [5, 6] and vegetation. The mineral laboratory samples were granular, with a particle diameter range of 250-1200μm. The fifth column shows that if there were no spectral atmospheric or illumination variation effects, the ratio of energies in band 1 to band 4 would permit discrimination of pyroxenes (found in basic and ultrabasic rocks), quartz (found in acidic rocks), limonite and hematite (iron

oxides), and green vegetation, on the basis of their respective ratio magnitudes. For instance, iron oxides and vegetation could be made to appear dark on the resulting ratio map, which would make pyroxene, as well as some other iron-containing minerals common to basic rocks, appear bright. Quartz would appear the same tone of gray as any other material which has a flat spectral curve in the visible-near IR wavelength region. A second ratio map, possibly utilizing the ratio of band 3 to band 4, could be used to discriminate between limonite and hematite, as is indicated by the sixth column of Table I. Not shown in Table I are carbonates with certain metallic ions, such as siderite (Fe), malachite (Cu), and smithsonite (Zn), which should also be discriminable from most other materials because of their deep spectral reflectance minima in the upper visible and reflective infrared wavelength regions.

3. GEOLOGICAL TEST SITE AND SCIENTIFIC OBJECTIVES

The region selected for this ERTS experiment is the southern end of the Wind River Range, Wyoming, as shown in Figure 3. Within the region of specific interest, the target of primary interest is the main iron formation member of the Golden Meadows formation. The main iron formation, averaging about 30% iron content [7], is composed of Precambrian laminated and thin-bedded deposits of chiefly quartz and magnetite and is located just North of Atlantic City, Wyoming. An attempt will be made to map these Precambrian iron deposits. To the Northwest is the Precambrian Louis Lake batholith, which is primarily biotite-hornblende quartz diorite and granodiorite, bordered by migmatite and gray gneiss. Interlaced within the batholith are diabasic gabbro dikes of widths on the order of 200-300 feet and lengths up to 10 miles. The gabbro contains more iron than the main body of the batholith; accordingly, an attempt will be made to detect exposed parts of these dikes on the basis of their higher iron content.

Other geological features within the specific region of interest include a Permian phosphoria formation (phospatic limestone, chert, shale and dolemite), the Mississippian Madison limestone formation, Precambrian granitic pegmatites (on the order of 1000 feet in diameter), and Tertiary deposits of calcareous conglomerate, volcanic ash, sand, and sandstone. These and other geological targets within the ERTS frame will be studied, with lower expectations of discriminability.

The objectives of this experiment also extend beyond the ones stated above. If successfully implemented, the ratio image technique should be helpful in the location of other iron, nickel, and copper deposits for which iron oxides may act as a surface expression of the ore, e.g., gossans. It should also be useful for various types of vegetation mapping, because a ratio of visible red to reflective infrared channels, or vice versa, greatly enhances the contrast between live vegetation and all other targets. Vegetation-soil mixtures may be estimable from such ratio images, which would prove useful for rangeland management, forestry, agriculture and other studies.

4. EXPERIMENTAL PLAN

Atmospheric effects and the spectral dependence of solar illumination will surely effect images produced from satellite data, however. It is primarily for this reason that ratioing has been chosen as the principal mode of data processing. The following data processing plan will explain why. The spectral radiance of Lambertian targets measured by the ERTS MSS scanner can be expressed as

$$L_\lambda = S\left(\frac{E_{sun_\lambda}}{\pi}\right)\tau_\lambda\rho_\lambda + L_{P_\lambda} \qquad (1)$$

where L_λ = measured spectral radiance,
S = shadow or illumination factor (1.0 for no shadow in instantaneous field of view),
E_{sun_λ} = spectral irradiance of the sun (impinging upon target),
τ_λ = atmospheric transmittance,
ρ_λ = spectral reflectance of target,
L_{P_λ} = path radiance (caused by atmospheric scattering).

The L_{P_λ} term contains path radiance from two sources: light scattered into the beam between target and detector, and light scattered off the sun-target direction (diffuse illumination), then reflected off the target toward the detector. Whenever the L_{P_λ} term is negligible, as with low-altitude scanner data on a clear day (such is the case for the data in Figure 1), all of the environmental factors are multiplicative. From satellite altitudes, however, L_{P_λ} is no longer negligible. To get rid of most or all of this additive term, one can take the purely empirical approach of dark object subtraction. In a shadowed region, $S = 0$ because there is no direct solar irradiance; hence $L_\lambda = L_{P_\lambda}$ whenever the shadow is large compared with a spatial resolution element. Note that a shadow caused by topographic relief is preferable to a cloud shadow for this purpose because there may be preferential spectral transmission (via selective scattering and absorption) through clouds, unless they are optically thick for all wavelengths measured. For a given spectral channel, the value of the lowest radiance measured within the scene can be subtracted from all other spatial resolution elements in the scene. Since the ERTS channels are spectrally relatively narrow, compared with spectral features of the solid targets, the approximation will be made that for the i^{th} channel,

$$L_i \approx L_{\lambda_i} \quad \Delta\lambda_i \qquad (2)$$

where λ_i is the median wavelength and $\Delta\lambda_i$ is the spectral width (at 50% transmission points) of the i^{th} channel. After dark object subtraction, the ratio of the i^{th} and $(i + 1)^{th}$ channels will be approximately

$$R_{i,i+1} \approx \frac{L_i}{L_{i+1}} = \frac{S\left(\frac{E_{sun_i}}{\pi}\right)\tau_i\rho_i}{S\left(\frac{E_{sun_{i+1}}}{\pi}\right)\tau_{i+1}\rho_{i+1}} \tag{3}$$

$$= \frac{E_{sun_i}}{E_{sun_{i+1}}} \quad \frac{\tau_i}{\tau_{i+1}} \quad \left(\frac{\rho_i}{\rho_{i+1}}\right)$$

In equation 3, the only term which should vary widely over an ERTS frame (for most geological test sites) is ρ_i/ρ_{i+1}, the target reflectance term. The ratio may not be invarient for a given type of target type in two ERTS frames collected at different times in different places, however. For a further suppression of environmental factors (S, E_{sun_i}, τ_i, and L_{P_i}), one can measure the spectral reflectance of a known target within the ERTS frame and use it as a reference, for which the ERTS-measured ratio would be:

$$(R_{i,\,i+1})_{reference} = \frac{E_{sun_i}}{E_{sun_{i+1}}} \quad \frac{\tau_i}{\tau_{i+1}} \quad \left(\frac{\rho_i}{\rho_{i+1}}\right)_{reference} \tag{4}$$

A division of equation 3 by equation 4 yields, after rearrangement,

$$\frac{\rho_i}{\rho_{i+1}} = \left(\frac{\rho_i}{\rho_{i+1}}\right)_{reference} \left[\frac{R_{i,i+1}}{(R_{i,i+1})_{reference}}\right] \tag{5}$$

from which the term ρ_i/ρ_{i+1} can be calculated almost independent of environmental factors. The "almost" is included in the foregoing statement because the degree of environmental independence is dependent on how well the dark object subtraction succeeds in suppressing the path radiance term. It should be noted that the dark object subtraction is an approximation, because part of the L_{P_λ} term is dependent on target reflectance. However, it is assumed here that the target reflectance dependence of L_{P_λ} is negligible. Should the above procedure yield poor results, i.e., fail to suppress atmos-

pheric effects, a theoretical approach will be attempted, whereby L_{p_λ} values calculated from an atmospheric model [8] will be employed to arrive at the ratios in equations 3 and 5. It should also be noted that the dark object subtraction method cannot be used to yield data from the darkest elements in the scene. These elements will be processed in a different manner, possibly as a straight radiance ratio.

All of these calculations will be accomplished on the IBM 7094 computer, then input to an imaging device, which at this time is planned to be The Unversity of Michigan SPARC analog computer. Development of the software for the experiment is underway, and hopefully will be completed by 1 January 1973.

5. CONCLUSIONS

An experimental plan for enhancing spectral features related to the chemical composition of geological targets in ERTS multispectral scanner data has been described. If this method proves successful it should prove useful for regional geologic mapping, mineralogical exploration, and soil mapping. It may also be helpful to ERTS users in scientific disciplines other than geology, especially to those concerned with targets composed of mixtures of live vegetation and soil or rock.

6. ACKNOWLEDGEMENTS

This work was supported by NASA contracts NAS-5-21783 and NAS-9-9784 and by U. S. Bureau of Mines contract HO220064. Conversations with J. Erickson, R. Nalepka, and R. Legault were useful and appreciated.

REFERENCES

1. "Rock-Type Discrimination from Ratioed Infrared Scanner Images of Pisgah Crater, California," R. K. Vincent and F. Thomson, Science, v. 175, pp. 986-988, 1972.

2. "Recognition of Exposed Quartz Sand and Sandstone by Two-Channel Infrared Imagery," R. K. Vincent, F. Thomson, and K. Watson, Journal of Geophysical Research, v. 77, pp. 2473-2477, 1972.

3. "Spectral Compositional Imaging of Silicate Rocks," R. K. Vincent and F. Thomson, Journal of Geophysical Research, v. 77, pp. 2465-2471, 1972.

4. "Experimental Methods for Geological Remote Sensing," R. K. Vincent, Fourth Annual Earth Resources Program Review, v. II, pp. 33-1 through 33-12, NASA Manned Spacecraft Center, Houston, Texas, 1972.

5. "Visible and Near-Infrared Spectra of Minerals and Rocks: I: Silicate Minerals," G. R. Hunt and J. W. Salisbury, Modern Geology, v. 1, pp. 283-300, 1970.

6. "Visible and Near-Infrared Spectra of Minerals and Rocks: III: Oxides and Hydroxides," G. R. Hunt, J. W. Salisbury and C. J. Lenhoff, submitted to Modern Geology, 1970.

7. "A Preliminary Report on the Precambrian Iron Deposits near Atlantic City, Wyoming," R. W. Bayley, USGS Bulletin 1142-C, pp. C1-C23, 1963.

8. R. Turner. University of Michigan, Willow Run Laboratories, private communications, 1972.

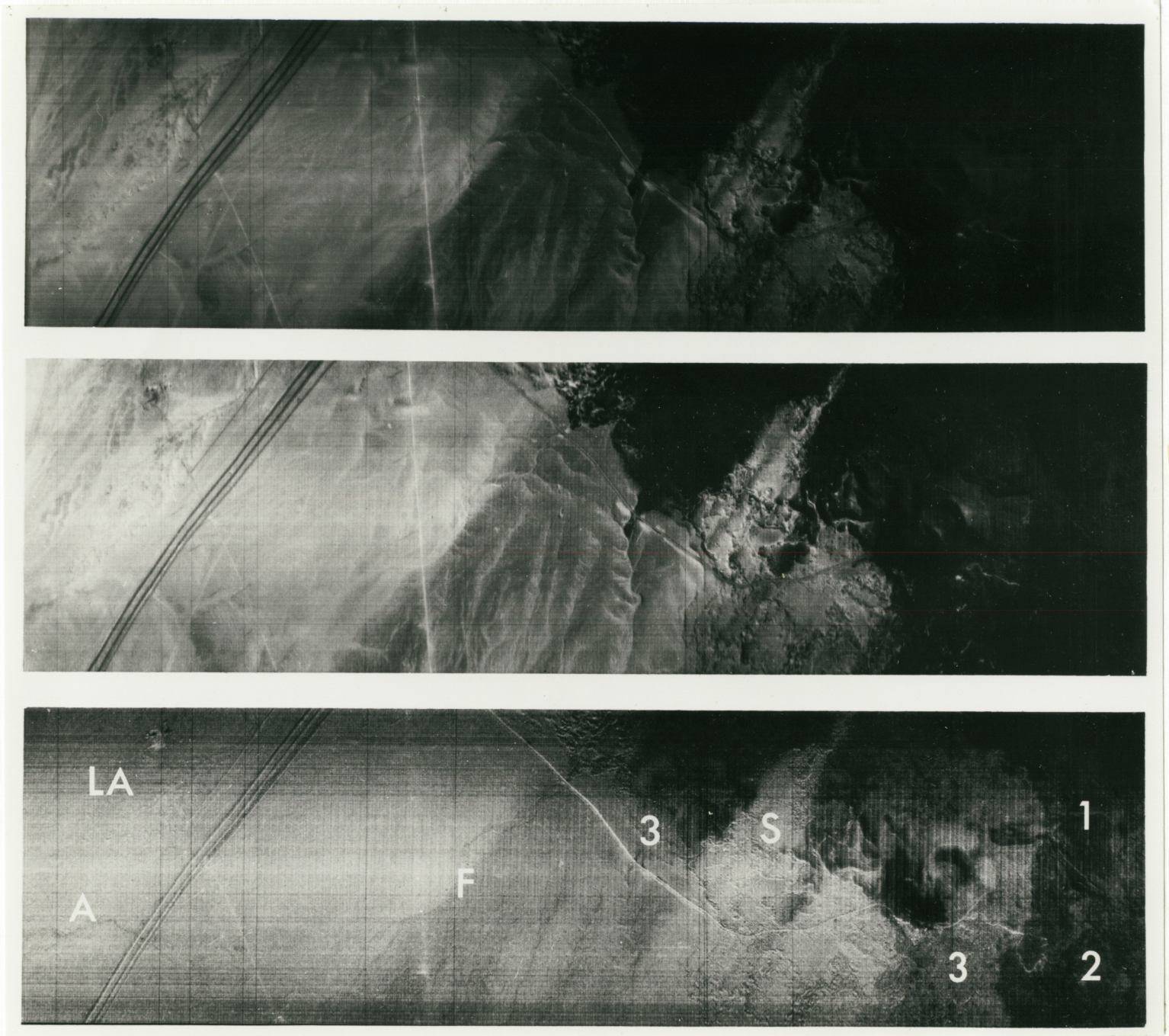

FIGURE 1. ANALOG VISIBLE AND REFLECTIVE INFRARED IMAGES OF FLIGHT LINE 1, SECTION A OF A NORTH-SOUTH FLIGHT OVER PISGAH CRATER, CALIFORNIA. (North is to the left.) Single channel images are at top (channel 5: 0.50-0.52μm) and middle (channel 7: 0.74-0.85μm); ratio image (channel 5/channel 7) is at bottom. Left to right: alluvium (A), aa lava partially buried by alluvium (LA); gravel and fanglomerate (F); windblown sand and silt (S); and three eruptive phases of Pisgah lava (1,2 and 3).

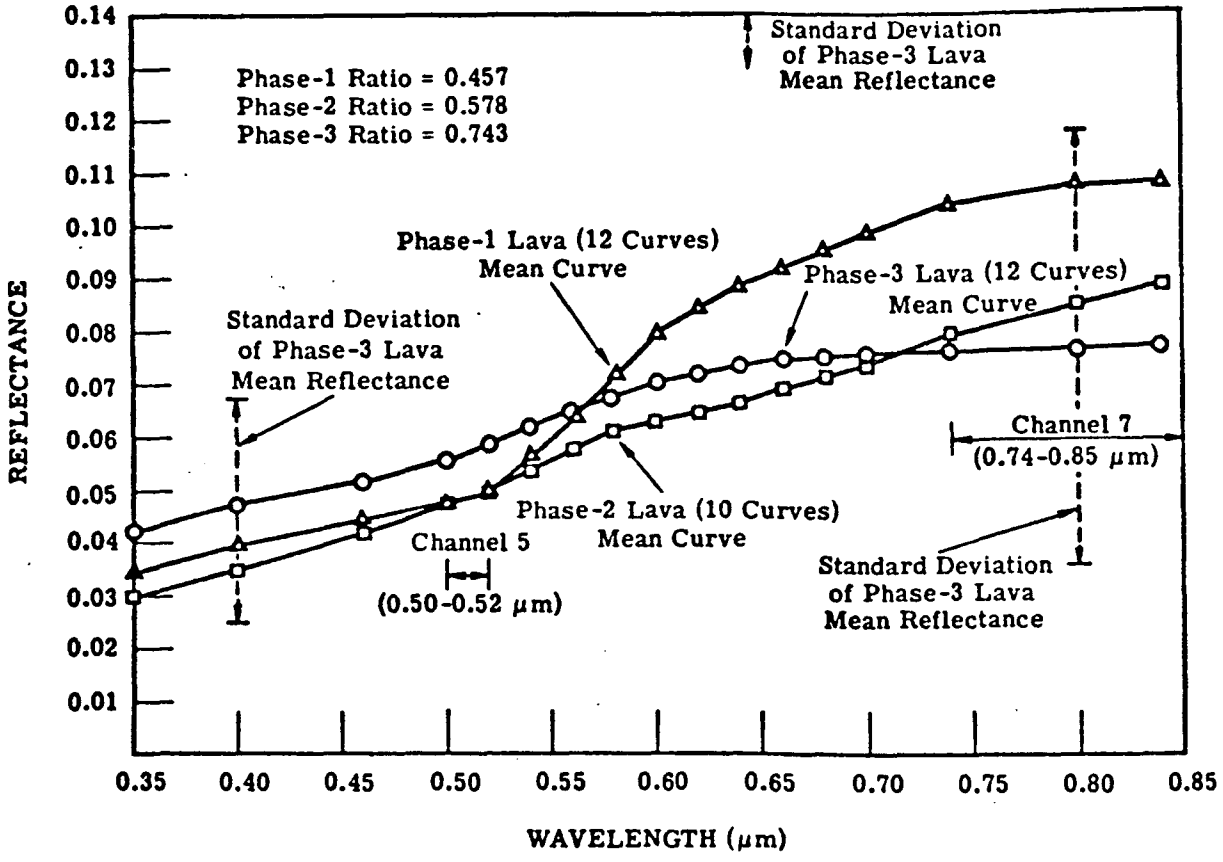

FIGURE 2. MEAN REFLECTANCE OF THREE LAVIC PHASES OF PISGAH CRATER BASALTS.

TABLE I. AVERAGE REFLECTANCE (RELATIVE TO MgO) OF TYPICAL SPECTRA OF VARIOUS MINERALS AND VEGETATION

NAME	Band 1 ρ_{ave_1} (0.5-0.6μm)	Band 2 ρ_{ave_2} (0.6-0.7μm)	Band 3 ρ_{ave_3} (0.7-0.8μm)	Band 4 ρ_{ave_4} (0.8-1.1μm)	$\frac{\rho_1}{\rho_4}$	$\frac{\rho_3}{\rho_4}$
Pyroxene (Diopside)	.37	.24	.16	.11	3.70	1.46
Quartz	.68	.70	.71	.73	1.07	.97
Limonite	.11	.30	.33	.29	0.38	1.14
Hematite	.09	.13	.17	.20	0.45	.85
Vegetation (Green)	.11	.13	.38	.47	0.23	.81

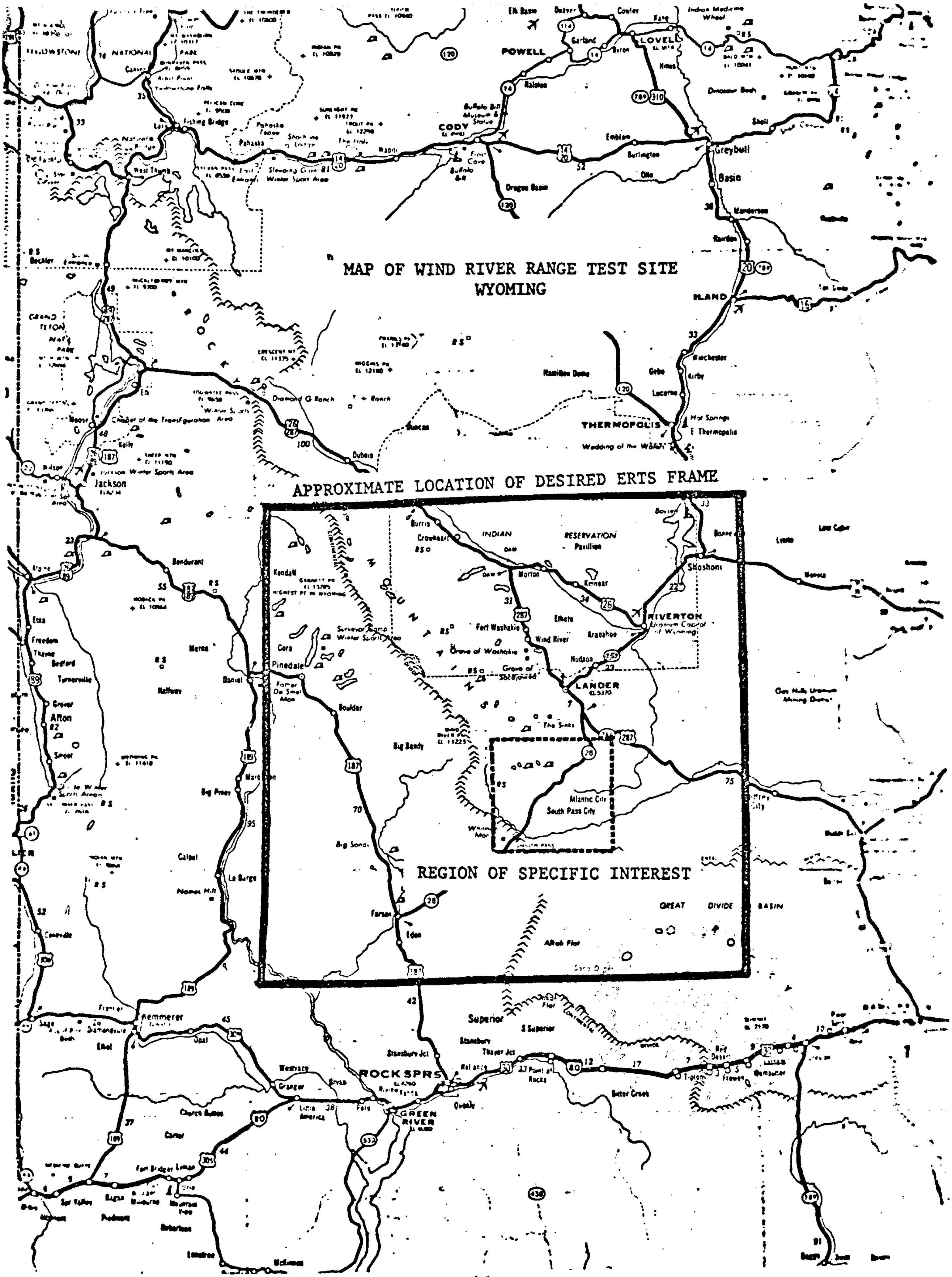
MAP OF WIND RIVER RANGE TEST SITE
WYOMING
APPROXIMATE LOCATION OF DESIRED ERTS FRAME
REGION OF SPECIFIC INTEREST
POWELL
CODY
Greybull
Basin
THERMOPOLIS
RIVERTON
LANDER
Shoshoni
Jackson
Pinedale
Boulder
Big Sandy
Farson
Eden
Atlantic City
South Pass City
GREAT DIVIDE BASIN
INDIAN RESERVATION
Kemmerer
Superior
ROCK SPRS
GREEN RIVER
Afton
Big Piney
La Barge
Dubois
Morton
Kinnear
Fort Washakie
Wind River
Hudson
Crowheart
Burris
Cora
Kendall
Daniel
Marbleton
Lovell
Emblem
Burlington
Hamilton Dome
Gebo
Kirby
Lucerne
Winchester
Hot Springs
E Thermopolis
Tipton
Point of Rocks
Granger
Little America
Fort Bridger
Lyman
Church Buttes
Carter
Bitter Creek
Opal
Freedom
Etna
Grover
Bedford
Thayne
Turnerville
Smoot
Calpet
Bondurant
Arapahoe
Ethete
Pavillion
Boysen
Manderson
Otto
Ralston
Garland
Byron
Cowley
Deaver
Dinosaur Beds
Shell
Kelly
Wilson
Hoback Jct
Moran
Elk
Alkali Flat
Wapiti
Lyman
Diamondville
Sage
Opal
Superior
Stansbury
Reliance
Quealy
Wamsutter
Red Desert
Table Rock
Creston
Alpine
Thayer Jct
Stansbury Jct
Westvaco
Burntfork
McKinnon
Lonetree
Robertson
Mountain View
Urie
Kemmerer
Frontier
Big Sandy
Diamond G Ranch
Chapel of the Transfiguration
Jackson Winter Sports Area
Surveyor Camp Winter Sports Area
Grave of Washakie
Grave of Sacajawea
The Sinks
Father De Smet Mon.
Uranium Capital of Wyoming
Gas Hills Uranium Mining District
Lost Cabin
Lysite
Moneta
Hiland
Ten Sleep
Kaycee
Emblem
Cody
Buffalo Bill Museum & Statue
Oregon Basin
Fishing Bridge
Yellowstone
National Park
Grand Teton Nat'l Park